Journal of Materials Chemistry C

Simple Molecular Ferroelectrics: *N,N'*-Dialkyl-terephthalamide Derivatives in Solid Phase

Journal:	*Journal of Materials Chemistry C*
Manuscript ID	TC-ART-10-2021-005001.R1
Article Type:	Paper
Date Submitted by the Author:	14-Jan-2022
Complete List of Authors:	Kawana, Moeko; Tohoku University, Graduate School of Engineering Mizoue, Ryohei; Tohoku University Graduate School of Engineering School of Engineering Takeda, Takashi; Tohoku University, Institute of Multidisciplinary Research for Advanced Materials Hoshino, Norihisa; Tohoku University Graduate School of Engineering School of Engineering, IMRAM, Tohoku Univ. Akutagawa, Tomoyuki; Tohoku University, Institute of Multidisciplinary Research for Advanced Materials

ARTICLE

Simple Molecular Ferroelectrics: *N,N'*-Dialkyl-terephthalamide Derivatives in Solid Phase

Received 00th January 20xx,
Accepted 00th January 20xx

DOI: 10.1039/x0xx00000x

Moeko Kawana,[a] Ryohei Mizoue,[a] Takashi Takeda,[a, b]* Norihisa Hoshino,[a, b] and Tomoyuki Akutagawa[a, b, c]*

Simple molecules of *N*,*N*'-dialkyl-1,4-benzenedicarboxamide (**CnIPA**) form a one-dimensional (1D) N−H•••O= hydrogen-bonding molecular assembly, which show a solid–solid phase transition through the partial melting of alkyl chains before phase transition to an isotropic liquid without the formation of a liquid crystal phase. The phase transition, molecular assembly structure, dielectric constant, and ferroelectricity of **CnTPA** were evaluated by changing the alkyl chain length (*n*) of $–CONHC_nH_{2n+1}$ through *n* = 5–16, 18. The 1D hydrogen-bonded structures were further assembled into a bilayer arrangement of alkyl chains to form a lamellar-type molecular assembly, where the partial melting of two alkyl chains occurred at the high-*T* solid phase. An even–odd effect was observed in the phase transition behavior and the *T*-dependent dielectric constants of **CnTPA**, where the even-number derivatives had much larger motional freedom than those of the odd-number derivatives. The dielectric response was associated with the motional freedom of the polar structural unit of N−H•••O= hydrogen bonds, the dynamics of which were activated in the *T* range after the phase transition to the high-*T* solid phase. The collective dipole inversion of the N−H•••O= hydrogen-bonding chain was observed in the ferroelectric polarization–electric field (*P*–*E*) hysteresis curves of **CnTPAs** with $n \geq 11$. The melting state of long alkyl chains in the high-*T* solid phase assisted the dipole inversion of N−H•••O= units to form hydrogen-bonded ferroelectrics.

Introduction

The variation range of intermolecular interactions in molecular assemblies can be chemically designed to form functional molecular materials. In addition to free molecular rotation, other types of motional freedom such as rotation of the $–CH_3$ group,[1] in-plane rotation of the π-planar molecule,[2–5] flip-flop rotation,[6–8] bowl-inversion,[9–11] proton transfer (PT),[12–16] and ionic displacement[9] have been observed in various of molecular assemblies. One important aspect is the coupling between these dynamics and the physical properties of the molecular assembly. For instance, ferroelectricity is an important physical response of dynamic molecular assemblies.[17–19]

Ferroelectric crystals can only be obtained from the 10 polar point groups without an inversion center, where the permanent dipole moment must be inverted by the application of an external electric field. Therefore, the chemical design of a dynamic crystalline environment is essential for the appearance of ferroelectricity based on the above polar crystals.[20, 21] Intermolecular PT in hydrogen-bonded molecular crystals has typically been utilized for designing ferroelectric molecular crystals.[22–24] The dynamics of charged H^+ inverted the direction of the dipole moment, where the change in crystal structures between the initial and the PT states remained quite small in magnitude to maintain the crystal lattice. Therefore, PT-type molecular ferroelectrics are a useful chemical approach for obtaining molecular ferroelectrics. In contrast, dynamical rotational environments in single crystals have been fabricated in molecular turnstiles,[25] molecular gyroscopes,[26–29] molecular gears,[30] and supramolecular rotators.[31–37] For instance, we have reported the supramolecular rotator structures of anilinium (Ani^+) and adamantylammonium ($ADNH_3^+$) on the stator of [18]crown-6 and dibenzo[18]crown-6 (DB[18]crown-6) in monovalent $[Ni(dmit)_2]^-$ single crystals.[6–8, 36, 37] A molecular design to introduce the polarity change for molecular rotation has been attempted to show a ferroelectric supramolecular rotator, where the flip-flop motion of *m*-$FAni^+$ on the DB[18]crown-6 stator realizes dipole inversion according to the flip-flop motion of polar F-groups in *m*-$FAni^+$(DB[18]crown-6)$[Ni(dmit)_2]^-$ single crystals.[38]

Another type of interesting ferroelectric liquid crystalline material has been reported in alkylamide ($–CONHC_nH_{2n+1}$)-substituted benzene derivatives, where the rotation of hydrogen-bonding polar alkylamide chains plays an essential role to show ferroelectricity.[39–41] For instance, an *N*, *N*, *N*''-trialkyl-1,3,5-benzenetricarboxamide (**3BC**) derivative showed ferroelectric *P*–*E* hysteresis curves in the discotic hexagonal columnar (Col_h) liquid crystal phase.[39–41] Hydrogen-bonding of the **3BC** molecule was first reported by Matsunaga *et al.* as a thermally stable Col_h liquid crystalline compound,[42] where the

[a] *Graduate School of Engineering, Tohoku University, Sendai 980-8579, Japan.*
[b] *Institute of Multidisciplinary Research for Advanced Materials (IMRAM), Tohoku University, 2-1-1 Katahira, Aoba-ku, Sendai 980-8577, Japan. E-mail:* akutagawa@tohoku.ac.jp and takashi@tohoku.ac.jp
[c] *National Institute for Material Science (NIMS), 1-2-1 Tsukuba, 305-0047, Japan.*
† Footnotes relating to the title and/or authors should appear here.
Electronic Supplementary Information (ESI) available: [details of any supplementary information available should be included here]. See DOI: 10.1039/x0xx00000x

intermolecular N−H•••O= hydrogen-bonding interaction forms the 1D columnar molecular assembly. In addition, the excellent organogellation ability of **3BC** was reported in the 3D entangled molecular assembly structure of a bundle of each 1D column.[43] The application of an external electric field along the 1D amide-type N−H•••O= hydrogen-bonding column in the Col_h phase aligned the direction of each dipole moment, where the polarization direction of the $(N-H•••O=)_\infty$ column was reversibly inverted by the external electric field. The 1D $(N-H•••O=)_\infty$ column has a macroscopic dipole moment along the hydrogen-bonding direction, and collective inversion is responsible for the *P*–*E* hysteresis curve. The ferroelectric alkylamide unit can be introduced into a variety of functional π-molecules. For instance, the π-expanded pyrene[44–46] and tetrabenzoporphyrin[47] bearing four $–CONHC_{14}H_{29}$ chains formed 1D ferroelectric hydrogen-bonding columns as well as a specific optical response simultaneously. Therefore, multifunctionality has been designed for various π-molecular systems using a rational design of hydrogen-bonding alkylamide chains. The photoresponsive trans–cis isomerization of azobenzene[48] and nonplanar helicene π-cores[49] have also been combined with hydrogen-bonding ferroelectricity using alkylamide chains to form lamellar-type liquid crystals. To design a multifunctional π-molecular system, the chemical design of the π-core is a useful technique to achieve hybrid ferroelectric properties.

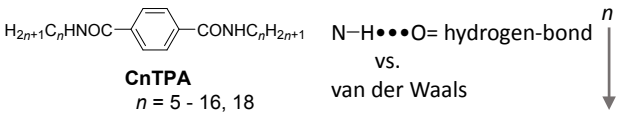

Scheme 1 Molecular structures of **CnTPA** (*n* = 5–16, 18). Compensation of the intermolecular N−H•••O= hydrogen-bonding and multiple van der Waals interactions at $–CONHC_nH_{2n+1}$ chains, which are adjustable by a systematic change of the structural parameter *n*.

A simple benzene derivative bearing multiple alkylamide chains is a useful structural unit for designing ferroelectricity in the Col_h liquid crystal phase. Interestingly, **3BC** and *N*, *N*′′, *N*′′′, *N*′′′′, *N*′′′′′-penta(tetradecyl)-1,2,3,4,5-benzenepentacarboxamide (**5BC**) derivatives indicated ferroelectric *P*–*E* hysteresis curves in the Col_h liquid crystal phase, whereas *N*, *N*′, *N*′′, *N*′′′-tetra(tetradecyl)-1,2,3,4,5-benzenetetracarboxamide (**4BC**) and *N*, *N*′, *N*′′, *N*′′′, *N*′′′′, *N*′′′′′ -hexa(tetradecyl)-1,2,3,4,5-benzenehexacarboxamide (**6BC**) showed antiferroelectric behavior.[50, 51] This difference is simply explained by the steric hindrance for the rotation of the nearest-neighboring $–CONHC_nH_{2n+1}$ chains at the benzene ring. In addition, the chemical design of the alkyl chains of **3BC** enables the formation of chiral molecular assemblies, where the introduction of (*R*)-3,7-dimethyloctylamide into **3BC** formed the same Col_h liquid crystal phase with almost the same phase transition behavior.[52, 53] However, chiral *N,N′,N*′′-tri-(*R*)-3,7-dimethyloctyl-1,3,5-tricarboxamide (***R*-3BC**) had a lower magnitude of the coercive electric field (E_c) for dipole inversion, by a fact of 10.[52, 53] The chemical design of alkylamide chains is a useful method for controlling the ferroelectric response. On the contrary, the much simpler molecular structure of *N*, *N*′-bis(tetradecyl)-1,4-benzenedicarboxamide (**C14TPA**) did not show the Col_h liquid crystal phase and had a solid–solid phase transition.[50] It was noted that **C14TPA** at the high-*T* solid phase exhibited a ferroelectric *P*–*E* hysteresis curve at 433 K, where the motional freedom of $–CONHC_{14}H_{29}$ chains and the dipole inversion of N–H•••O= hydrogen bonds occurred at the high-*T* solid phase. The solid-state dynamics of the two $–CONHC_{14}H_{29}$ chains contributed to the appearance of ferroelectricity; however, the dipole inversion mechanism of **C14TPA** in the high-*T* solid phase has not been sufficiently examined. To understand the dipole inversion mechanism of **C14TPA** in solids, we examined the alkyl amide chain length (*n*) dependence of **CnTPA** derivatives for *n* = 5–16 to 18 (Scheme 1). The *n*-dependent dynamics of alkylamide chains and the dipole inversion of hydrogen-bonded N–H•••O= units in the molecular assembly were evaluated in terms of the phase transition behavior, molecular assembly structure, dielectric constant, and ferroelectric *P*–*E* hysteresis of **CnTPAs**. The molecular assembly of **CnTPA** is mainly fabricated by N–H•••O= hydrogen-bonding interactions and van der Waals interactions at the alkyl chains. Thus, the elongation of the *n*-number increases the contribution from the van der Waals interaction, which affects the dynamic behavior of the N–H•••O= hydrogen-bonding interaction and its inversion and its inversion.

Results and discussion

Phase transition behaviors

TG diagrams of all **CnTPA** derivatives (*n* = 5–16, 18) showed a considerably high thermal stability up to 500 K in the absence of weight loss after the phase transition to an isotropic liquid (IL) (Fig. S1). Larger *n*-number derivatives have higher thermal decomposition temperatures. The melting points of **CnTPA** before thermal decomposition were observed in the *T*-range of 450–490 K, where the derivatives of longer *n*-number indicated lower melting points. Fluidic behavior was not observed in all **CnTPAs** before the melting points, in the absence of a liquid crystal phase. However, solid–solid phase transitions before the melting point were observed in all **CnTPAs** in the DSC charts (Figs. S2 and S3). Fig. 1a shows the DSC curves of **C7TPA** (black), **C13TPA** (red), and **C16TPA** (blue). The relatively short-chain compound of **C7TPA** had two phase transitions, S1–S2 at 379 K and S2–IL at 479 K, of which the changes in transition enthalpy (ΔH) were 11.0 and 50.5 kJ mol^{-1}, respectively (Table S1). With the elongation of the *n*-number to **C13TPA**, there appeared three kinds of solid–solid phase transitions, S1–S2 at 380 K (ΔH = 17.2 kJ mol^{-1}), S2–S3 at 454 K (ΔH = 9.5 kJ mol^{-1}), and S3–IL at 460 K (ΔH = 54.3 kJ mol^{-1}) in the heating process, where the S3 phase was not observed in the cooling process. Further elongation of *n*-number to **C16TPA** revealed the high-*T* S4 phase together with S1, S2, and S3 phases, and the S1–S2, S2–S3, S3–S4, and S4–IL phase transitions were observed at 393 K (ΔH = 38.9 kJ mol^{-1}), 437 K (ΔH = 16.5 kJ mol^{-1}), 445 K (ΔH = 10.3 kJ mol^{-1}), and 450 K (ΔH = 50.56 kJ mol^{-1}) in the heating process,

respectively. The molecular assembly structures of **CnTPA** have a tendency to undergo successive phase transitions by increasing the *n*-number.

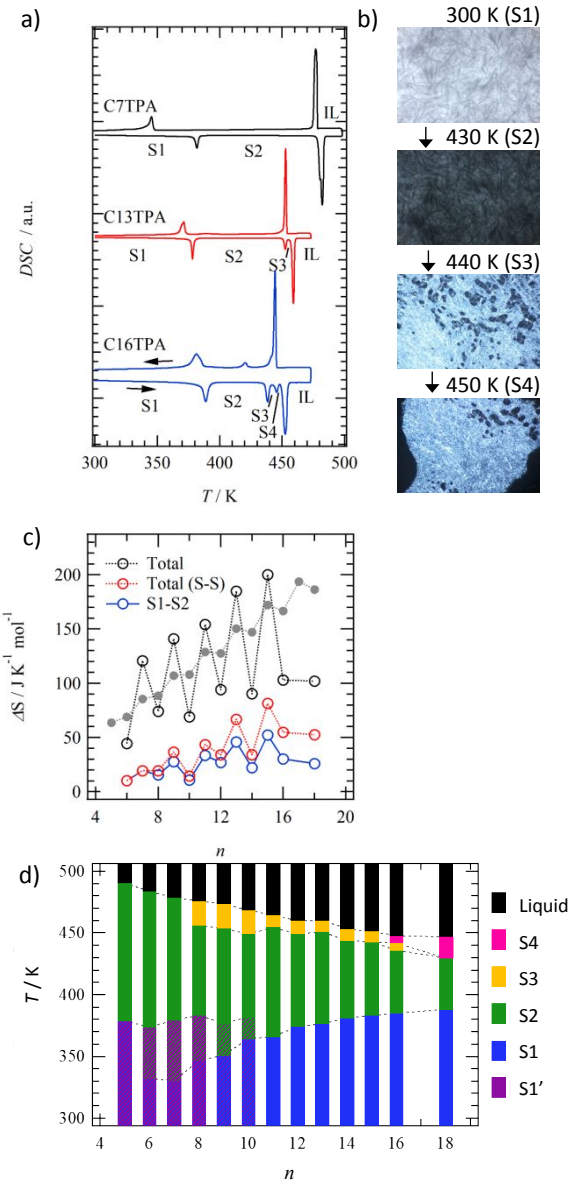

Fig. 1 *n*-dependent phase transition behaviors of **CnTPA**. a) DSC charts of **C7TPA** (black), **C13TPA** (red), and **C16TPA** (blue). b) POM images of **C16TPA** at 300 K (S1), 430 K (S2), 440 K (S3), and 450 K (S4) in the heating process. c) Even–odd effect of transition enthalpy change (ΔS) of S1–S2 phase transition (blue), sum of all solid–solid phase transitions $\Sigma\Delta S_{S\text{-}S}$ (red), total $\Sigma\Delta S$ for all solid–solid phase transition including solid–IL one (black), and theoretical $\Sigma\Delta S$ for *n*-alkane crystals (gray). d) *n*-dependent phase diagram.

Fig. 1b summarizes the polarized optical microscopy (POM) images of **C16TPA** under the cross-Nicole optical arrangement. The phase transition from microcrystalline S1 to the high-*T* S2 phase slightly modulated the POM image, accompanied by a subtle plasticity without fluidic behavior. Further heating of the S2 phase resulted in two additional S3 and S4 phases, where bright birefringence with nonfluidic behavior was observed without the liquid crystal phase. In these phase transitions, the thermally activated motional freedom of alkylamide chains plays an important role, where both the N–H · · · O= hydrogen-bonding and multiple van der Waals interactions effectively contribute to the crystal lattice energy of **CnTPA**.

Fig. 1c summarizes the *n*-dependent phase transition entropy change (ΔS) of **CnTPAs** (Table S1). The ΔS value from the highest solid phase to IL was larger than that of the other solid–solid phase transitions, suggesting that partial melting of the two alkylamide chains occurred in solid–solid phase transitions. The even–odd effect was observed in ΔS values for the S1–S2 phase transition, the sum of all solid–solid phase transitions $\Sigma\Delta S_{S\text{-}S}$, and total $\Sigma\Delta S_{all}$ for all solid–solid phase transitions, including the solid–IL transition (Fig. S4). The odd-number **CnTPAs** had a much larger ΔS value than those of the corresponding even-number derivatives. The even–odd effect for the solid–solid phase transitions and melting point is associated with a difference in the intermolecular interactions at the terminal $-CH_3$ groups. For instance, the even-numbered *n*-alkane crystals have much higher melting points than those of the corresponding odd-number ones, which has been explained by the densely packed structures in the even–number crystals.[52-56] This difference has been discussed from the orientation change for the two terminal $-CH_3$ groups, where the molecular symmetries of the even- and odd-number C_nH_{2n+2} molecules are C_i and C_2, respectively. Therefore, the two $-CH_3$ groups of the even-numbered *n*-alkane crystals are arranged in an anti-parallel orientation, resulting in a dense packing structure. The odd-number **CnTPAs** had relatively larger ΔS values than those of the even-numbered **CnTPAs**, indicating that the packing structure of the odd-number **CnTPAs** became much denser than the even-numbered **CnTPAs**. Two $-C_nH_{2n+1}$ chains were elongated along the long axis of the **CnTPA** molecule, where the alkyl chain formed a bilayer structure and interacted with the terminal $-CH_3$ groups (see the section on molecular assemblies).

Fig. 1d summarizes the *n*-dependent phase transition diagram of **CnTPAs**. The S1 and S2 phases were observed in the *n*-number range of $5 \le n \le 7$, while the S1, S2, and S3 phases were confirmed in the *n*-number range of $8 \le n \le 15$. The additional S4 phase found in $n = 16$ and 18 indicated a large conformational freedom of the two long alkylamide chains in **C16TPA** and **C18TPA**. The S1–S2 phase transition of all **CnTPAs** was observed around 370 K, and the S2 phase was exited in a relatively wide *T* range, whereas high-*T* S3 and S4 phases appeared in a narrow *T*-range before the melting point. A much longer *n*-number of **CnTPA** indicated the presence of high-*T* crystal S3 and S4 phases. The ΔS values for the S1–S2 phase transition mainly contributed to the sum of all solid–solid phase transitions (Fig. 1c). The conformational change of the alkyl chains mainly occurred during the first S1–S2 phase transition, and further structural modulation contributed to S3 and S4 phase transitions. The ΔS value of the solid–IL phase transition had the same magnitude as the sum of all solid–solid phase transitions ($\Sigma\Delta S$), and the total magnitude of $\Sigma\Delta S_{all}$ tended to follow the melting ΔS of *n*-alkanes. The dissociation of all N–H•••O= hydrogen-bonding interactions and the complete

melting of alky chains contributed to the total $\Sigma\Delta S$ value for solid–solid and solid–IL phase transitions. Therefore, approximately a half unit of alkyl chains has conformational freedom after the phase transition to the S2 state.

Molecular assembly structures

To evaluate the molecular assembly structures of **CnTPA**, single-crystal X-ray structural analysis of **C5TPA** was conducted at 250 K. It was difficult to obtain high-quality single crystals with **CnTPAs** with $n > 5$. Fig. 2a shows the unit cell of **C5TPA** viewed along the *b*-axis. Two amide units of the **C5TPA** molecule elongated at the trans-orientation to the benzene π-core with an all-trans alkyl conformation (Fig. S5). The π-planes of the nearest-neighboring benzene rings did not effectively overlap with each other in the absence of the formation of the π-stacking column (Fig. S6). In contrast, the 1D double N–H•••O= hydrogen-bonded chains connected each **C5TPA** molecule along the *a*-axis, where the interatomic N–O distance of $d_{N\text{-}O}$ = 2.9802(3) Å formed a 1D tape-like hydrogen-bonding array. The 1D hydrogen-bonding tapes and layers of alkyl chains were alternately arranged along the *c*-axis, forming a 2D lamellar-like molecular assembly structure. A bilayer-type arrangement of the alkyl chains was observed in the *ab* plane. The amide-type N–H•••O= hydrogen bonding and van der Waals interactions dominated the packing structure of **C5TPA**.

The S1–S2 and S2–IL phase transitions of **C5TPA** were observed at 379 and 489 K, respectively, during the heating process. Fig. 2b summarizes the *T*-dependent PXRD patterns of **C5TPA**, together with the simulated PXRD pattern based on single-crystal X-ray structural analysis at 100 K. The PXRD patterns of **C5TPA** at 293 and 353 K (S1 phase) were almost the same as the simulated pattern at 100 K, except for the observation of the low-angle reflection peak at 2θ = 3.99° and the intense peak at 2θ = 5.22°. The *d*-spacings of these two peaks corresponded to 22.1 and 17.0 Å, respectively, where the latter intense reflection peak was in accordance with the length of the *c*-axis of 16.8328(18) Å in the single-crystal X-ray structural analysis. After the phase transition to S2 phase, one intense reflection peak at 2θ = 4.10° was observed in the d_{001} = 21.5 Å at 473 K. In the cooling process from phase S2 to S1, two reflection peaks of d_{001} = 22.0 Å and d_{001}' = 16.9 Å were again reversibly observed at 323 K, where the d_{001}'-spacing was consistent with the length of the *c*-axis along the interlayer periodicity based on the single-crystal X-ray structural analysis at 250 K. On the contrary, the interlayer d_{001}-spacing of the S2 phase was elongated by approximately 5 Å along the *c*-axis through the thermal expansion of the crystal lattice, in contrast with the interlayer d_{001}-spacing in the S1 phase. In the low-*T* S1 phase, two different interlayer d_{001} periodicities for the S1 and S2 phases coexist in the molecular assembly.

The formation of the 1D hydrogen-bonded molecular assembly was confirmed in the SEM images of **C15TPA** at the spin-coating film on the HOPG substrate surface (Fig. 2c). Although the gelation ability of **CnTPA** was not observed in common organic solvents, the dilute solution of **C15TPA** in $CHCl_3$ formed fibrous microcrystals with a width of 500 nm and length of 10 μm. The amide-type N–H•••O= double hydrogen-bonding interaction appeared in the 1D microcrystal morphologies of **C15TPA**, which was consistent with the single-crystal X-ray crystal structural analysis of **C5TPA**.

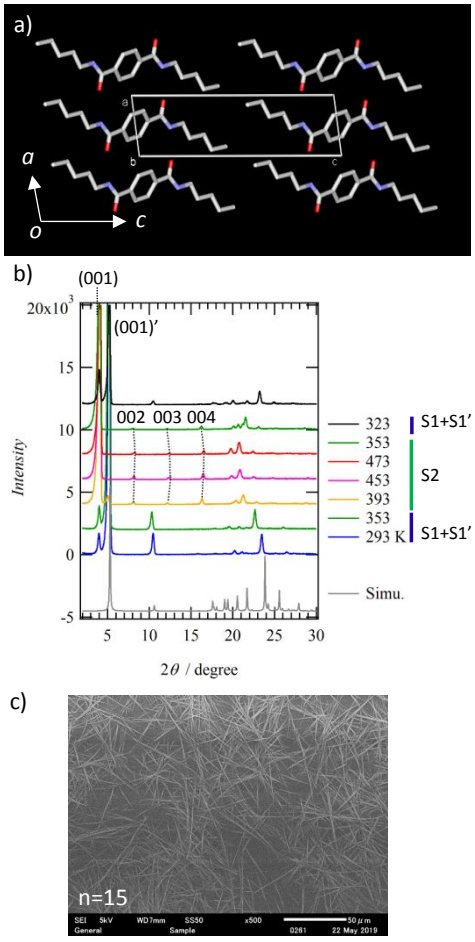

Fig. 2 Molecular assembly structure of **CnTPA**. a) Unit cell of **C5TPA** viewed along the *b*-axis based on single-crystal X-ray structural analysis at 250 K. b) *T*-dependent PXRD patterns of **C5TPA** for S1 (or S1') and S2 phases with the simulated PXRD pattern based on single-crystal X-ray structural analysis. c) SEM image of the 1D fibrous microcrystals of **C15TPA** on the HOPG substrate surface.

The same PXRD patterns of all **CnTPAs** with $n \geq 5$ suggested the formation of a layered lamella-type molecular assembly structure (Figs. S7–S8). Fig. 3a shows the *T*-dependent PXRD patterns of **C13TPA** in the S1 and S2 phases. The low-angle intense Bragg reflection peaks of **C13TPA** at 2θ = 2°–7° at 298 K were assigned to the layer spacing of d_{001}, d_{002}, and d_{003} indexes, resulting in the interlayer *d*-spacing of 40.3 Å without the additional d_{001}' reflection peak. After the phase transition to S2 phase, the interlayer d_{001} reflection peak was observed at a slightly elongated length of d_{001} = 42.1 Å at 403 K. In the discotic liquid crystalline phase, a drastic decrease in the d_{001} spacing was commonly observed in the phase transition from solid, where the long alkyl chains were completely melted and interdigitated.[57] Such complete melting behavior of alkyl chains was not observed in the S1–S2 phase transition of **CnTPA**. The thermally activated partial melting behavior of the two alkyl chains slightly modulated the interlayer d_{001} spacing in the high-

T S2 phase. On the contrary, the high-angle reflection pattern around $2\theta = 20°–25°$ for the S2 phase was different from that at the S1 phase. A sharp reflection peak at $2\theta = 23.0°$ at 298 K was completely diminished after the phase transition to the S2 phase at 393 K, where a broad reflection peak around $2\theta = 20°$ overlapped with sharp Bragg reflection peaks. The appearance of such a broad diffraction peak around $2\theta = 20°$ corresponded to the thermal melting state of the alkyl chains, which was clearly confirmed in long alkyl chain derivatives of **CnTPAs** with $n \geq 10$ (Figs. S8, S9). However, the broad peak around $2\theta = 20°$ was not clearly confirmed in the short alkyl chain derivative of **C5TPA** in the S2 phase, suggesting a small magnitude of thermal melting of $-C_5H_{11}$ chains in contrast with that of **C13TPA**. A linear correlation between the interlayer d_{001} (and d_{001}') spacing and *n*-number was clearly observed in all **CnTPAs** with $n \geq 5$ at 298 K (Fig. 3b). Among them, **C13TPA** had only the d_{001} reflection peak without the additional d_{001}' one, whereas all other **CnTPAs** showed both the d_{001} and d_{001}' reflection peaks simultaneously (Figs. S7–S9). The coexistence of two kinds of interlayer spacing in the S1 phase was commonly observed in **CnTPAs**, except for **C13TPA**.

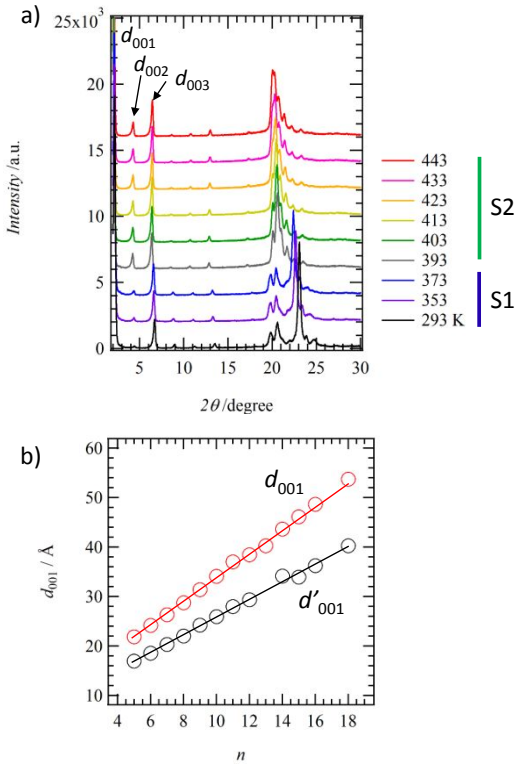

Fig. 3 Molecular assembly structure of **CnTPA**. a) *T*-dependent PXRD patterns of **C13TPA** at S1 and S2 phases. b) *n*-number dependence for the interlayer d_{001} and d_{001}' spacing at 298 K (S1 phase).

Dielectric responses

The *T*- and frequency (*f*) dependent dielectric constants are useful indicators for evaluating the dynamic motion of the polar structural unit in the molecular assembly.[58] The thermally activated motion of the polar hydrogen-bonded N–H · · · O= units can be detected in dielectric measurements, whereas the motional freedom of alkyl chains without the change in dipole moment is inert with respect to the dielectric spectra. Figs. 4a and 4b show the *T*- and *f*-dependent ε_1 changes in even-number **C12TPA** and odd-number **C13TPA**, respectively. Although the same hydrogen-bonding lamellar-type molecular assemblies were confirmed for both compounds, there was a drastic difference in their ε_1 responses. The ε_1 values around ~3 showed *T*- and *f*-independent behavior at the S1 phase of **C12TPA**, and the S1–S2 phase transition slightly decreased the ε_1 values. Above 380 K, a clear *T*- and *f*-dependent ε_1 response was observed with increasing *T*, where a larger ε_1 enhancement was observed at lower *f*-conditions and the slow molecular motions of polar structural units occurred at the S2 phase of **C12TPA**. The motional freedom of the polar N–H · · · O= hydrogen-bonding units and the partial melting behavior of the alkyl chains were thermally activated in the S2 phase of **C12TPA**. A similar trend for the *f*-dependent ε_1 enhancement was observed for the even-number **C14TPA**. In contrast, the dielectric constants of $\varepsilon_1 \sim 4.0$ at the S1 phase of **C13TPA** were inert after the phase transition to the S2 phase above 375 K, where a gradual *f*-independent ε_1 lowering was observed above 398 K. The S1–S2 phase transition temperature of **C13TPA** was inconsistent with the temperature at which the ε_1 anomaly appeared, and the *f*-dependences for even-number **C12TPA** and odd-number **C13TPA** were different from each other. Similar ε_1–*T* behaviors were also observed for odd-numbered **C11TPA** and **C15TPA** (Figs. S17 and S21) The even- and odd-number alkyl chain lengths affected the *T*- and *f*-dependent dielectric responses, which was consistent with the even–odd effect on the strength of hydrogen-bonding interactions found in the vibrational spectra (see the section on the ferroelectric mechanism).

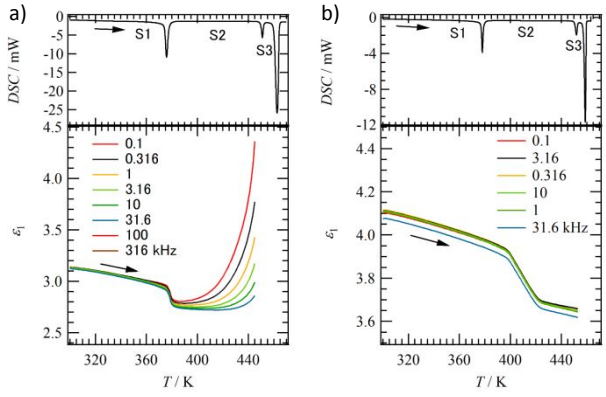

Fig. 4 *T*- and *f*-dependent ε_1 responses of a) even-number **C12TPA** and b) odd-number **C13TPA** together with DSC traces in the heating process.

Fig. 5 summarizes the *n*-dependent ε_1–*T* plots at a fixed frequency of $f = 100$ Hz. All ε_1 values of **CnTPAs** at 300 K were observed in the ε_1-range of 1.3–4.2, and *T*- and *n*-dependent changes were associated with the thermally activated motional freedom N–H•••O= hydrogen-bonding interactions (Figs. S11–S23). The ε_1–*T* plots of **CnTPAs** with n = 5–8 showed ε_1

enhancement at the S1–S2 phase transition temperatures with relatively low ε_1 values around 1.3–2.0, with increasing *T*. On the contrary, a nearly *T*-independent ε_1 behavior was observed at odd-number **C9TPA** without the ε_1 anomaly at the S1–S2 phase transition at 383 K. However, a relatively large ε_1 response was observed at even-number **C10TPA**, where the ε_1 value at 450 K was approximately 4 times higher than that at 300 K without the ε_1 anomaly at the S1–S2 phase transition temperature (390 K). Similar *T*-dependent ε_1 enhancements with increasing *T* were observed for even-numbered **C12TPA** and **C14TPA**. The ε_1–*T* plots of **C11TPA**, **C13TPA**, **C15TPA**, **C16TPA**, and **C18TPA** indicated a ε_1-drop by increasing in *T* after the phase transition to the S2 phase. Among them, a relatively sharp ε_1-drop was observed in the even-numbered **C14TPA**, **C16TPA**, and **C18TPA**, whose anomaly temperatures were nearly consistent with the S1–S2 phase transition temperatures. On the contrary, ε_1-drops for odd-numbered **C11TPA**, **C13TPA**, and **C15TPA** were observed at a broad change, and the temperatures were inconsistent with the S1–S2 phase transition temperatures. After the phase transition to the S2 phase, the ε_1 values of these odd-number **CnTPAs** indicated a gradual drop in the absence of a clear *f*-dependence. The *n*-number and even–odd effect of the two alky chains on **CnTPAs** influenced the dielectric responses and the motional freedom of the polar N–H•••O= hydrogen-bonding structures in the molecular assembly. The ε_1–*T* responses of **CnTPA** with $n \geq 10$ were larger than those with $n < 10$, suggesting much larger thermally activated motional freedom in the longer alkyl chain derivatives at the high-*T* solid phases of S2, S3, and S4.

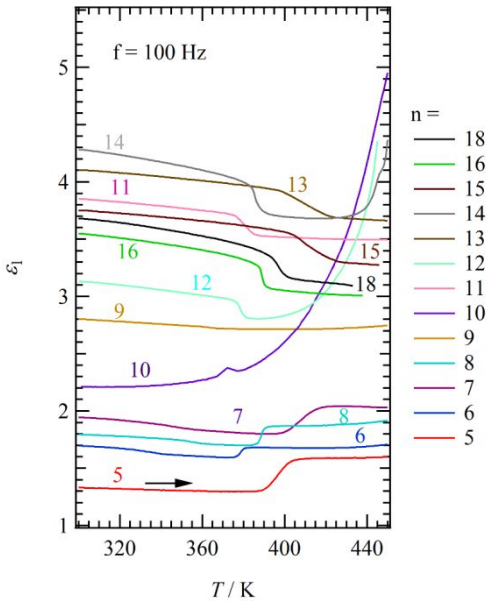

Fig. 5 *n*-dependent ε_1–*T* plots of **CnTPA** at a fixed frequency of *f* = 100 Hz.

Ferroelectric properties

The ε_1 responses of **CnTPAs** with $n \geq 10$ were different from those of the shorter alkyl chain derivatives. The appearance of ferroelectricity was evaluated for all **CnTPAs**, which was associated with the thermally activated motional freedom of the collective inversion of (N–H · · · O=)$_\infty$ hydrogen-bonding chains. Figs. 6a and 6b show the *T*- and *f*-dependent *P*–*E* hysteresis curves of **C15TPA**. The S1–S2, S2–S3, and S3–IL phase transitions of **C15TPA** were observed at 383, 428, and 452 K, respectively, during the heating process. Ferroelectric *P*–*E* hysteresis loops were observed in the high-*T* S2 phase at *T* = 413 and 423 K, while similar ferroelectric *P*–*E* hysteresis curves were also confirmed at the S3 phase at 433 and 443 K. However, there was no *P*–*E* hysteresis behavior in the temperature range of the S1 phase, owing to freezing of the thermally activated motional freedom of the –CONHC$_n$H$_{2n+1}$ chains. Therefore, the ferroelectricity of **C15TPA** appeared in the high-*T* solid S2 and S3 phases. The magnitude of remanent polarization (P_r) of 1.1 μC cm^{-2} at 423 K for the S2 phase was half the magnitude of P_r = 2.8 μC cm^{-2} at 443 K for the S3 phase, although the coercive electric field (E_c) at both the S2 and S3 phases were almost the same at 31.5 and 30.4 V μm^{-1}, respectively. The *f*-dependent *P*–*E* hysteresis curves of **C15TPA** at 443 K (S2 phase) indicated a much larger P_r value under much slower *f* conditions with almost the same E_c values. The P_r value of 2.84 μC cm^{-2} at *f* = 0.1 Hz was approximately 4 times larger than that of P_r = 0.66 μC cm^{-2} at *f* = 1.0 Hz, suggesting the occurrence of a slow dipole inversion in the S2 and S3 phases. Ferroelectric *P*–*E* hysteresis curves were observed for **CnTPAs** with $n \geq 11$ (Figs. S25–S27), whereas clear ferroelectric *P*–*E* hysteresis behaviors were not observed in the short alkyl chain derivatives of **CnTPA** with $n \leq 10$. The absolute magnitude of P_r = 2.3 μC cm^{-2} at 453 K for the S3 phase of **C14TPA** (*f* = 0.1 Hz) was larger than that of P_r = 1.7 μC cm^{-2} at 443 K for the S2 phase (*f* = 0.1 Hz), which corresponded to the larger amplitude of the motional freedom for the polar hydrogen-bonding unit at the S3 phase than that at the S2 phase. A large leak current showed insufficient *P*–*E* hysteresis curves for **C10TPA** (Fig. S30). Short alkyl chain **CnTPAs** with $n < 10$ are insufficient to allow sufficient magnitude of thermal motion for the polar N–H•••O= units in hydrogen-bonded molecular assemblies. The P_r values of the S2 phase for **C11TPA**, **C12TPA**, **C13TPA**, **C14TPA**, **C15TPA**, **C16TPA**, and **C18TPA** were 1.24, 2.00, 1.67, 2.84, 1.56, and 1.91 μC cm^{-2} at *f* = 0.1 Hz, respectively, where the even–odd effect was observed in these P_r values. The thermally activated motional freedom of the polar N–H · · · O= hydrogen-bonding units was affected by the *n*-number of alkyl chains in the lamellar-type molecular assembly.

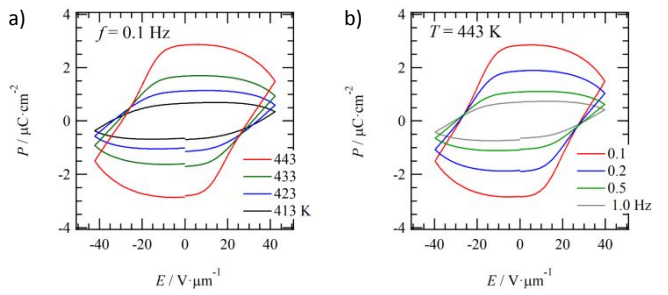

Fig. 6 *P*–*E* hysteresis curves of **C15TPA**. a) *T*-dependent *P*–*E* curves at *f* = 0.1 Hz and b) *f*-dependent *P*–*E* hysteresis curves at 443 K.

Mechanism of ferroelectricity in solids

None of the **CnTPAs** showed a phase transition to the liquid crystal phase, although solid–solid phase transitions were observed with increasing *T*. The N–H•••O= hydrogen-bonded 1D molecular assembly of **CnTPA** with $n \geq 11$ exhibited ferroelectricity as well as an even–odd effect in the phase transition, dielectric constant, and ferroelectric P_r value. The ferroelectricity of **CnTPAs** has been observed in the high-*T* solid S2, S3, and S4 phases before melting to the IL phase. The dipole inversion in the ferroelectric phase was associated with the collective inversion of the 1D intermolecular N–H•••O= hydrogen bonds, which was assisted by the partial melting behavior of two $-C_nH_{2n+1}$ chains above the S2 phase. To clarify the N–H•••O= hydrogen-bonding interaction of **CnTPAs**, the *T*-dependent vibrational IR spectra of KBr pellets were measured to determine the energy change of N–H•••O= hydrogen-bonding interactions around the S1–S2 phase transition (Figs. S37–S41).

Figs. 7a and 7b show the *T*-dependent energy change of the asymmetrical N–H stretching mode ($\nu_{N\text{-}H}$, cm^{-1}) of the intermolecular N–H•••O= hydrogen bonds for **C14TPA** and **C15TPA**, respectively, together with the DSC traces during the heating process. The energy of the $\nu_{N\text{-}H}$ mode in the solution phase showed a much higher energy $\nu_{N\text{-}H}$ band at 3520 cm^{-1}. The much stronger N–H•••O= hydrogen-bonding interaction yielded a red-shift of the energy of the $\nu_{N\text{-}H}$ mode, while the much weaker one showed a blue shift of the $\nu_{N\text{-}H}$ mode. The S1–S2 phase transition of **C14TPA** was observed at 380 K during the heating process, while the energy of the $\nu_{N\text{-}H}$ mode indicated *T*-independent behavior at 3334 cm^{-1} through the *T* range from 298 to 400 K. The S1–S2 phase transition in the DSC charts was mainly governed by the partial melting behavior of the two $-C_nH_{2n+1}$ chains, whose temperature was inconsistent with the temperature at which the energy shift of the $\nu_{N\text{-}H}$ mode occurred. After the partial melting behavior of the two $-C_nH_{2n+1}$ chains, the structural reconstruction of the polar N–H•••O= hydrogen-bonding interaction was thermally activated at a temperature approximately 20 K higher than that of the S1–S2 phase transition temperature. The energy of the mode $\nu_{N\text{-}H}$ = 3338 cm^{-1} of **C14TPA** at 403 K indicated a sudden drop of 25 cm^{-1} to 3313 cm^{-1} at 423 K in the S2 phase as *T* increased. It was noted that the energy of the N–H•••O= hydrogen bond in the low-*T* S1 phase suggested the formation of a much stronger hydrogen-bonding interaction at the high-*T* S2 phase than that at the S1 phase, owing to the partial melting behavior of the two alkyl chains. During the cooling process, a large thermal hysteresis of the energy of the $\nu_{N\text{-}H}$ mode was reversibly observed from 3308 cm^{-1} at 393 K (S2 phase) to 3339 cm^{-1} at 383 K (S1 phase), which was almost consistent with the S1–S2 phase transition temperature in the cooling process of the DSC chart. The temperature required to activate the motional freedom of the polar N–H•••O= hydrogen bonds was inconsistent with the partial melting temperature of the alkyl chains in the DSC measurements. The *T*-dependent energy shift of the $\nu_{N\text{-}H}$ mode for odd-number **C15TPA** (Fig. 7b) also revealed a similar behavior to that of even-number **C14TPA**. The S1–S2 phase transition temperature (383 K) in the DSC chart was 20 K higher than the temperature at which the $\nu_{N\text{-}H}$ drop occurred (403 K), where the energy of the mode $\nu_{N\text{-}H}$ = 3337 cm^{-1} at 300 K (S1 phase) was 26 cm^{-1} shifted to 3313 cm^{-1} at 413 K (S2 phase). Thermal hysteresis behavior was also observed in the heating and cooling cycles of the $\nu_{N\text{-}H}$ mode for **C14TPA**, and the temperature of the $\nu_{N\text{-}H}$ shift in the cooling process was almost the same as the S2–S1 phase transition temperature. Similar reversible $\nu_{N\text{-}H}$ anomalies and thermal hysteresis behaviors were observed in all **CnTPAs** around the S1–S2 phase transition (Figs. S37–41).

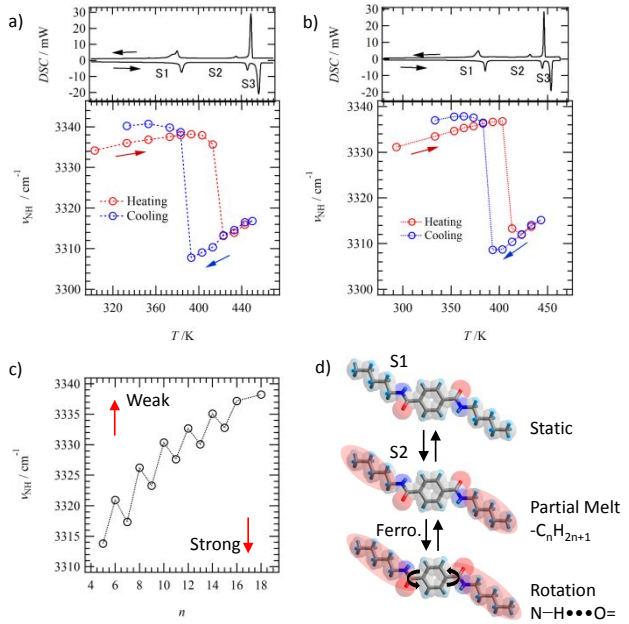

Fig. 7 Phase transition behavior and mechanism of ferroelectricity for **CnTPA** with $n > 10$. *T*-depedent energy shift of $\nu_{N\text{-}H}$ mode for a) **C14TPA** and b) **C15TPA** on KBr pellets in the heating and cooling process together with the DSC trace. c) *n*-dependent energy shifts of $\nu_{N\text{-}H}$ mode at 298 K. d) Phase transition mechansim to ferroelectric state and the motional freedom of $-CONHC_nH_{2n+1}$ chains at S1 and S2 phases.

Fig. 7c summarizes the *n*-dependent $\nu_{N\text{-}H}$ mode of **CnTPA** at 298 K. The even–odd effect was clearly observed in the *n*-dependent energy shifts of the $\nu_{N\text{-}H}$ modes. Alternating strong and weak N–H•••O= hydrogen-bonding interactions were confirmed in the energy shifts of the $\nu_{N\text{-}H}$ modes (Fig. S38), where the even-number **CnTPAs** had a much higher energy $\nu_{N\text{-}H}$ mode than those of odd-number **CnTPAs**. The $\nu_{N\text{-}H}$ modes of **C6TPA** and **C18TPA** were observed at 3321 and 3338 cm^{-1}, respectively, where the elongation of the *n*-number resulted in a blue shift of the $\nu_{N\text{-}H}$ modes. Therefore, the elongation of *n*-number in **CnTPAs** tended to weaken the N–H•••O= hydrogen-bonding interaction, which is consistent with the appearance of ferroelectricity by the application of external stimuli. The even–odd effect of N–H•••O= hydrogen-bonding energy was consistent with the phase transition enthalpy, *T*-dependent dielectric constant, and P_r value of **CnTPAs**. A much lower $\nu_{N\text{-}H}$

mode indicated a much stronger intermolecular N−H•••O= hydrogen-bonding interactions in the odd-number **CnTPAs**, which decreased the sum of $\Sigma\Delta S$ for the even-numbered **CnTPAs**. The much larger *T*- and *f*-dependent ε_1 responses of even-number **CnTPAs** were also consistent with the formation of much weaker N−H•••O= hydrogen-bonding interactions, where the weak N−H•••O= hydrogen-bonding interaction increased the N−O distance and dipole moment. Therefore, the P_r value of the even-numbered **CnTPAs** became larger than those of the odd-numbered **CnTPAs**. In contrast, the effective N−H•••O= hydrogen-bonding interaction for the odd-number **CnTPAs** increased the $\Sigma\Delta S$ value and suppressed the *T*- and *f*-dependent ε_1 response and the P_r value.

Fig. 7d shows a schematic view of the thermally activated molecular motions of **CnTPAs** with increasing *T*. The static S1 phase transformed to the dynamic S2 phase, where the partial melting of alkyl chains occurred and the N−H•••O= hydrogen-bonding interaction became stronger than that at the S1 phase. However, the motional freedom of N−H•••O= hydrogen bonds was not activated at the S1–S2 phase transition temperature in the DSC charts. After the phase transition to the S2 phase, dipole inversion could be activated to produce a ferroelectric response in the *P*–*E* hysteresis curves. The thermal motion of the partially melted alkyl chains supported the dissociation of N−H•••O= hydrogen-bonding interactions and the appearance of ferroelectricity.

Conclusions

The hydrogen-bonded *N*, *N*'-dialkyl-1,4-benzenedicarboxamide (**CnTPA**) formed solid-state ferroelectrics according to the alkyl chain length *n*. The phase transition behavior, molecular assembly structure, dielectric constant, and ferroelectric response were examined for 13 kinds of **CnTPAs** with *n* = 5–16, 18. All **CnTPAs** showed solid–solid and solid–isotropic liquid phase transitions without the formation of a liquid crystal phase. When the *n*-number of **CnTPA** was greater than 8, three types of solid phases (S1, S2, and S3) were observed before the melting point, and the additional S4 phase was confirmed at **C16TPA** and **C18TPA**. The first S1–S2 phase transition resulted in partial melting of the alkyl chains, followed by the complete melting of the alkyl chains and the dissociation of N−H•••O= hydrogen bonds occurred at the melting point. The sum of all transition enthalpies $\Sigma\Delta S$ showed an even–odd effect for the melting of alkyl chains of **CnTPAs**, where the $\Sigma\Delta S$ value for the odd-number derivatives became higher than that of the even ones. The 1D N−H•••O= hydrogen-bonding chains were confirmed in the single-crystal X-ray structural analysis of **C5TPA**, while the two alkyl chains formed a lamella-type bilayer structure with the aid of hydrophobic interactions. The *T*- and *f*-dependent dielectric constants revealed the differences in the even- and odd-number **CnTPAs** in the motional freedom of the polar structural unit of N−H•••O= hydrogen bonds, where the even-number **CnTPAs** with $n \geq 12$ showed much larger dielectric enhancement under high-*T* and low-*f* conditions. Both the packing structure and the motional freedom of N−H•••O= hydrogen bonds and van der Waals interactions between alkyl chains were affected by the *n* number. Notably, ferroelectric *P*–*E* hysteresis curves were observed for long-chain derivatives of **CnTPAs** with $n \geq 11$, where the P_r values of the even-numbered **CnTPA** were larger than those of the odd-numbered ones. In the S2 phase, the N−H•••O= hydrogen-bonding structure was reconstructed by the partial melting of the alkyl chains, which was consistent with the *T*-dependent vibrational spectra. The dynamics of the alkyl chains were confirmed by the solid–solid phase transition behavior, whereas the dynamics of N−H•••O= hydrogen bonds were observed in the *T*-dependent dielectric constants and IR spectra. The packing structure and magnitude of the intermolecular interaction of **CnTPA** were influenced by the even–odd effect and dielectric responses. Coupling between the motional freedom of alkyl chains and N−H•••O= hydrogen-bonding interactions determined the solid-state ferroelectric response of **CnTPA** with $n \geq 11$. The elongation *n*-number decreased the strength of the N−H•••O= hydrogen-bonding interaction, which enabled the ferroelectric *P*–*E* hysteresis curves to be observed. The chemical design of simple benzene derivatives enables the formation of environmentally friendly solid-state ferroelectrics without the use of rare earth metals. The control of multiple intermolecular interactions plays an important role in achieving a dipole inversion environment in solids and ferroelectricity. A variety of organic ferroelectrics have the potential to design high-density and flexible memory devices. Among them, the simplicity of the molecular structure is an important design strategy for obtaining new organic ferroelectrics. The chemical design of plastic crystalline-like materials is a useful approach for forming dynamic polar structural units in molecular assemblies.

Conflicts of interest

There are no conflicts to declare.

Acknowledgements

This work was supported by a Grant-in-Aid for Scientific Research on KAKENHI (Grant Numbers: JP19H00886, JP20H05865, JP20K05442, and JP20H04655), Japan Science and Technology Agency, Core Research for Evolutional Science and Technology (Grant Number: JPMJCR18I4), and the "Dynamic Alliance for Open Innovation Bridging Human, Environment and Materials" project supported by the Ministry of Education, Culture, Sports, Science and Technology.

Notes and references

1 T. Atake, H. Gyoten, H. A. Chihara, *J. Chem. Phys*. 1982, **76**, 5535–5540.
2 T. Inabe, Y. Matsunaga, Y. Yoshida, *Bull. Chem. Soc. Jpn*. 1979, **52**, 615–616.
3 J. Ichikawa, N. Hoshino, T. Takeda, T. Akutagawa, *J. Am. Chem. Soc*. 2015, **137**, 13155−13160.
4 Y. Yoshida, Y. Shimizu, T. Yajima, G. Maruta, S. Takeda, Y. Nakano, T. Hiramatsu, H. Kageyama, H. Yamochi, G. Saito, *Chem. Eur. J*. 2013, **19**, 12313–12324.

5 J. Harada N. Yoneyama S. Sato Y. Takahashi T. Inabe, *Cryst. Grow. Des*. 2019, **19**, 291–299.
6 S. D. Karlen, H. Reyes, R. E. Taylor, S. I. Khan, M. F. Hawthorne, M. A. Garcia-Garibay, *Proc. Natl. Acad. Sci. U. S. A*. 2010, **107**, 14973–14977.
7 I. Liepuoniute, C. M. Huynh, S. Perez-Estrada, Y. Wang, S. Khan, K. H. Houk, M. A. Garcia-Garibay, *J. Phys. Chem. C* 2020, **124**, 15391–15398.
8 A. Colin-Molina, M. J. Jellen, E. Garcìa-Quezada, M. E. Cifuentes-Quintal, F. Murillo, J. Barroso, S. Perez-Estrada, R. A. Toscano, G. Merino, B. Rodrìguez-Molina, *Chem. Sci*., 2019, **10**, 4422–4429.
9 D. Miyajima, K. Tashiro, F. Araoka, H. Takezoe, J. Kim, K. Kato, M. Takata, T. Aida, *J. Am. Chem. Soc*. 2009, **131**, 44–45.
10 Y. Shoji, T. Kajitani, F. Ishiwari, Q. Ding, H. Sato, H. Anetai, T. Akutagawa, H. Sakurai, T. Fukushima, *Chem. Sci*. 2017, **8**, 8405–8410.
11 S. Furukawa, J. Wu, M. Koyama, K. Hayashi, N. Hoshino, M. Saito, T. Akutagawa, *Nature Commun*. 2021, **12**, 768−1−9.
12 G. Saito, Y. Matsunaga, *Bull. Chem. Soc. Jpn*., 1971, **44**, 3328–3335.
13 T. Mitani, G. Saito, H. Urayama, *Phys. Rev. Lett*. 1988, **60**, 2299−2302.
14 T. Isono, H. Kamo, A. Ueda, K. Takahashi, A. Nakao, R. Kumai, N. Nakao, K. Kobayashi, Y. Murakami, H. Mori, *Nature Commun*. 2013, **4**, 1344–1–6.
15 T. Akutagawa, G. Saito, *Bull. Chem. Soc. Jpn*. 1995, **68**, 1753−1773.
16 T. Akutagawa, G. Saito, M. Kusunoki, K. Sakaguchi, *Bull. Chem. Soc. Jpn*. 1996, **69**, 2487−2511.
17 *Ferroelectric Memories*. J. F. Scott, ed., Springer. 2000.
18 *Principles and Applications of Ferroelectrics and Related Material*, M. E. Lines, A. M. Glass eds., Oxford University Press, New York, 1977.
19 F. Jona, G. Shirane, *Ferroelectric Crystals*. Dover Publications Inc., NY, 1993.
20 T. Akutagawa, *Bull. Chem. Soc. Jpn*. 2021, **94**, 1400–1420.
21 T. Akutagawa, T. Takeda, N. Hoshino, *Chem. Comm*. 2021, **57**, 8378–8401.
22 A. Katrusiak, M. Szafrański, *Phys. Rev. Lett*. 1999, **82**, 576–579.
23 T. Akutagawa, S. Takeda, T. Hasegawa, T. Nakamura, *J. Am. Chem. Soc*. 2004, **126**, 291–294.
24 S. Horiuchi, Y. Tokunaga, G. Giovannetti, S. Picozzi, H. Itoh, R. Shimano, R. Kumai, Y. Tokura, *Nature* 2010, **463**, 789–792.
25 T. C. Bedard, J. S. Moore, *J. Am. Chem. Soc*. 1995, **117**, 10662–10671
26 M. A. Garcia-Garibay, *Proc. Natl. Acad. Sci. U. S. A*. 2005, **102**, 10771–10776.
27 C. S. Vogelsberg, M. A. Garcia-Garibay, *Chem. Soc. Rev*. 2012, **41**, 1892–1910.
28 Z. Dominguez, H. Dang, M. J. Strouse, M. A. Garcia-Garibay, *J. Am. Chem. Soc*. 2002, **124**, 7719–7727.
29 P. Commins, M. A. Garcia-Garibay, *J. Org. Chem*. 2014, **79**, 1611−1619.
30 M. J. Jellen, I. Liepuoniute, M. Jin, C. G. Jones, S. Yang, X. Jiang, H. M. Nelson, K. N. Houk, M. A. Garcia-Garibay, *J. Am. Chem. Soc*. 2021, **143**, 7740–7747.
31 T. Akutagawa, K. Shitagami, S. Nishihara, S. Takeda, T. Hasegawa, T. Nakamura, Y. Hosokoshi, K. Inoue, S. Ikeuchi, Y. Miyazaki, K. Saito, *J. Am. Chem. Soc*. 2005, **127**, 4397–4402.
32 S. Nishihara, T. Akutagawa, D. Sato, S. Takeda, S. Noro, T. Nakamura, *Chem. Asian J*. 2007, **2**, 1083–1090.
33 T. Akutagawa, T. Nakamura, *Dalton Trans*., 2008, **2008**, 6335–6345.
34 T. Akutagawa, H. Koshinaka, Q. Ye, S. Noro, J. Kawamata, H. Yamaki, T. Nakamura, *Chem. Asian J*., 2010, **5**, 520–529.
35 N. Hoshino, Y. Yoshii, K. Kubo, M. Aonuma, Y. Nakamura, T. Akutagawa, *Inorg. Chem*. 2012, **51**, 12968–12975.
36 D. Sato, T. Akutagawa, S. Takeda, S. Noro, T. Nakamura, *Inorg. Chem*. 2007, **46**, 363–365.
37 T. Akutagawa, D. Sato, H. Koshinaka, M. Aonuma, S. Noro, S. Takeda, T. Nakamura, *Inorg. Chem*. 2008, **47**, 5951–5962.
38 T. Akutagawa, H. Koshinaka, D. Sato, S. Takeda, S. Noro, H. Takahashi, R. Kumai, Y. Tokura, T. Nakamura, *Nature Mater*. 2009, **8**, 342–347.
39 C. F. C. Fitié, W. S. Roelofs, M. Kemerink, R. P. Sijbesma, *J. Am. Chem. Soc*. 2010, **132**, 6892–6893.
40 C. F. C. Fitié, W. S. C. Roelofs, P. C. M. M. Magusin, M. Wübbenhorst, M. Kemerink, R. P. Sijbesma, *J. Phys. Chem. B*. 2012, **116**, 3928–3937.
41 I. Urbanaviciute, S. Bhattacharjee, M. Biler, J. A. Lugger, M. T. D. Cornelissen, P. Norman, M. Linares, R. P. Sijbesma, M. Kemerink, *Phys. Chem. Chem. Phys*. 2019, **21**, 2069–2079.
42 Y. Matsunaga, N. Miyajima, Y. Nakayasu, S. Sakai, M. Yonenaga, *Bull. Chem. Soc. Jpn*. 1988, **61**, 207–210.
43 Y. Yasuda, E. Iishi, H. Inada, Y. Shirota, *Chem. Lett*. 1996, **25**, 575–576.
44 H. Anetai, Y. Wada, T. Takeda, N. Hoshino, S. Yamamoto, M. Mitsuishi, T. Takenobu, T. Akutagawa, *J. Phys. Chem. Lett*. 2015, **6**, 1813–1818.
45 H. Anetai, T. Takeda, N. Hoshino, Y. Araki, T. Wada, S. Yamamoto, M. Mitsuishi, M. Tsuchida, T. Ogoshi, T. Akutagawa, *J. Phys. Chem. C*. 2018, **122**, 6323–6331.
46 H. Anetai, K. Sambe, T. Takeda, N. Hoshino, T. Akutagawa, *Chem. Eur. J*. 2019, **25**, 11233–11239.
47 J. Wu, T. Takeda, N. Hoshino, Y. Suzuki, J. Kawamata, T. Akutagawa, *J. Phys. Chem. C*. 2019, **123**, 22439–22446.
48 J. Wu, Q. Zhu, T. Takeda, N. Hoshino, T. Akutagawa, *ACS Applied Electro. Mater*., 2021, **3**, 3521−3529.
49 H. Anetai, T. Takeda, N. Hoshino, H. Kobayashi, N. Saito, M. Shigeno, M. Yamaguchi, T. Akutagawa, *J. Am. Chem. Soc*. 2019, **141**, 2391–2397.
50 Y. Shishido, H. Anetai, T. Takeda, N. Hoshino, S.-i Noro, T. Nakamura, T. Akutagawa, *J. Phys. Chem. C*. 2014, **118**, 21204–21214.
51 J. Wu, T. Takeda, N. Hoshino, T. Akutagawa, *J. Phys. Chem. B*. 2020, **124**, 7067–7074.
52 L. Brunsveld, A. P. H. J. Schenning, M. A. C. Broeren, H. M. Janssen, J. A. J. M. Vekemans, E. W. Meijer, *Chem. Lett*. 2000, 292–293.
53 J. Wu, T. Takeda, N. Hoshino, Y. Suzuki, J. Kawamata, T. Akutagawa, *J. Mater. Chem. C*. 2020, **8**, 10283–10289.
54 D. F. R. Gilson, *J. Chem. Edu*. 1992, **69**, 23–25.
55 R. Boese, H. –C. Weiss, D. Bläser, *Angew. Chem. Int. Ed*. 1999, **38**, 988–992.
56 M. Sorai, K. Tsuji, H. Suga, S. Seki, *Mol. Cryst. Liq. Cryst*. 1980, **80**, 33–58.
57 T. Wöhrle, I. Wurzbach, J. Kirres, A. Kostidou, N. Kapernaum, J. Litterscheidt, J. C. Haenle, P. Staffeld, A. Baro, F. Giesselmann, S. Laschat, *Chem. Rev*. 2016, **116**, 1139–1241.
58 K. C. Kao, *Dielectric Phenomena in Solids*. Elsevier: Amsterdam, 2004.